Pergamon

J. Mech. Phys. Solids, Vol. 43, No. 10, pp. 1615–1638, 1995
Elsevier Science Ltd
Printed in Great Britain

0022–5096(95)00038–0

DYNAMIC FAILURE MECHANISMS OF CERAMIC BARS: EXPERIMENTS AND NUMERICAL SIMULATIONS

H. D. ESPINOSA

School of Aeronautics and Astronautics, Purdue University, West Lafayette, IN 47907-1282, U.S.A.

and

N. S. BRAR

Impact Physics Laboratory, University of Dayton Research Institute, Dayton, OH 45469, U.S.A.

(*Received* 19 *November* 1994; *in revised form* 26 *March* 1995)

ABSTRACT

Failure mechanisms in ceramics are investigated by means of bar impact experiments and numerical simulations of the wave propagation event. Stress histories are measured by embedding manganin stress gauges in the ceramic bars. The fracture event is examined by high speed photography. A violent radial expansion, in a region close to the impact surface, followed by a cloud of debris is observed. Numerical simulations of the inelastic wave propagation event are performed with a multiple-plane microcracking model. The simulations show that when the impact stress exceeds a material threshold, the stress wave in the bar has a relatively short duration which is controlled by the rate of unconfined compressive damage. A nonzero inelastic strain rate at the wave front is required in the simulations to properly capture the measured stress attenuation with propagation distance. This feature is related to a heterogeneous material microstructure which is a common occurrence in ceramics. Furthermore, the simulations predict a radial expansion of the bar as a result of not only compressive but also tensile damage. The radial velocity histories on the bar surface are functions of wave propagation distance and damage rate. Tensile damage is induced by stress release from the rod surface and is restricted to the bar core, due to wave focusing, and to the bar free end. In the latest case, reflection of the compressive pulse produces bar spallation. The two dimensional distribution of tensile and compressive damage is assessed by means of contour plots of volumetric strain and the second invariant of the inelastic strain tensor.

1. INTRODUCTION

Recently, significant improvements have been made towards understanding dynamic compressive strength of brittle materials (Rosenberg *et al.*, 1988; Kipp and Grady, 1989; Espinosa and Clifton, 1991; Espinosa *et al.*, 1992; Brar and Bless, 1992; Grady and Wise, 1993). Nonetheless, uncertainties about the dominant failure mechanisms as a function of stress states still remain. Espinosa *et al.* (1992) have shown that aluminas containing a glassy phase at grain boundaries can deform inelastically by flow of these thin glass layers at compressive stress levels well below the Hugoniot elastic limit of the material. The role of microstructural heterogeneities in the dynamic behavior of aluminas has also been pointed out by Longy and Cagnoux (1989), and Yeshurun *et al.* (1987). The material microstructure, porosity, grain size, and the

fraction and type of second phase, appear to play an even more critical role in the dynamic compressive strength of TiB_2 ceramics (Winkler and Stilp, 1992; Grady and Wise, 1993). A double-yield process has been observed in this material, although the mechanisms responsible for this behavior remain undetermined.

In an effort to investigate more general multiaxial loading conditions, Brar and Bless (1992), and Grady and Wise (1993) performed unconfined and confined ceramic bar experiments. The objective of these experiments is to extend uniaxial strain deformation states imposed in plate impact experiments. The possibility of generating a variety of multiaxial deformation states appears to be very relevant in the characterization of failure mechanisms in ceramics and ceramic composites. Espinosa (1994) has shown that the dramatic softening observed in these materials under pressure-shear states can be explained by accumulation of inelastic strain in a single orientation.

Despite the availability of experimental data documenting the brittle failure of ceramics, very few quantitative investigations have been performed addressing the role of microstructural features in the observed failure mechanisms. In the present work the unconfined bar experiments are examined by performing nonlinear wave propagation simulations based on a multiple-plane microcracking model. Stress histories measured with embedded gauges are compared with the model predictions to assess the relevance of compressive damage and its rate. Stress decay with distance of wave propagation is correlated to elastic dispersion and initial flaw size. Moreover, high speed photographs are compared to the predicted damage distribution within the bar and its radial expansion. The microcracking model provides good agreement with all the relevant features experimentally measured.

In this investigation a parametric study of failure in brittle materials due to dynamic microfracture is performed. The study would be of considerable interest in the following:

(i) Clarification of the mechanisms leading to the observed material failure and its dependence on grain size, second phases, and manufacturing processes.
(ii) Assessment of the role of damage induced anisotropy and pressure in the compressive behavior of brittle materials.
(iii) Development of guidelines for a better characterization of these materials including the selection of measurable quantities and their locations based on their sensitivity to damage and inelasticity. This aspect is of particular relevance in high-resolution velocity interferometry diagnostics.

2. EXPERIMENTAL METHOD AND RESULTS

2.1. *Experimental configuration*

Two types of alumina bars were used in the study. The first type were 12.7 mm diameter AD-998 and AD-94 sintered alumina bars manufactured by Coors Porcelain Company, Golden, CO. These bars were supplied by the manufacturer in 30.5 cm long pieces. The other type of bars were cored through the thickness of $30.5 \times 30.5 \times 7.6$ cm thick Coors AD-995 slabs. The surfaces of both types of bar were finely ground to a smooth finish and there were no visible surface flaws. The experimental configuration is shown in Fig. 1. Manganin gauges (Type C-880113, Micro-Measurements, Raleigh,

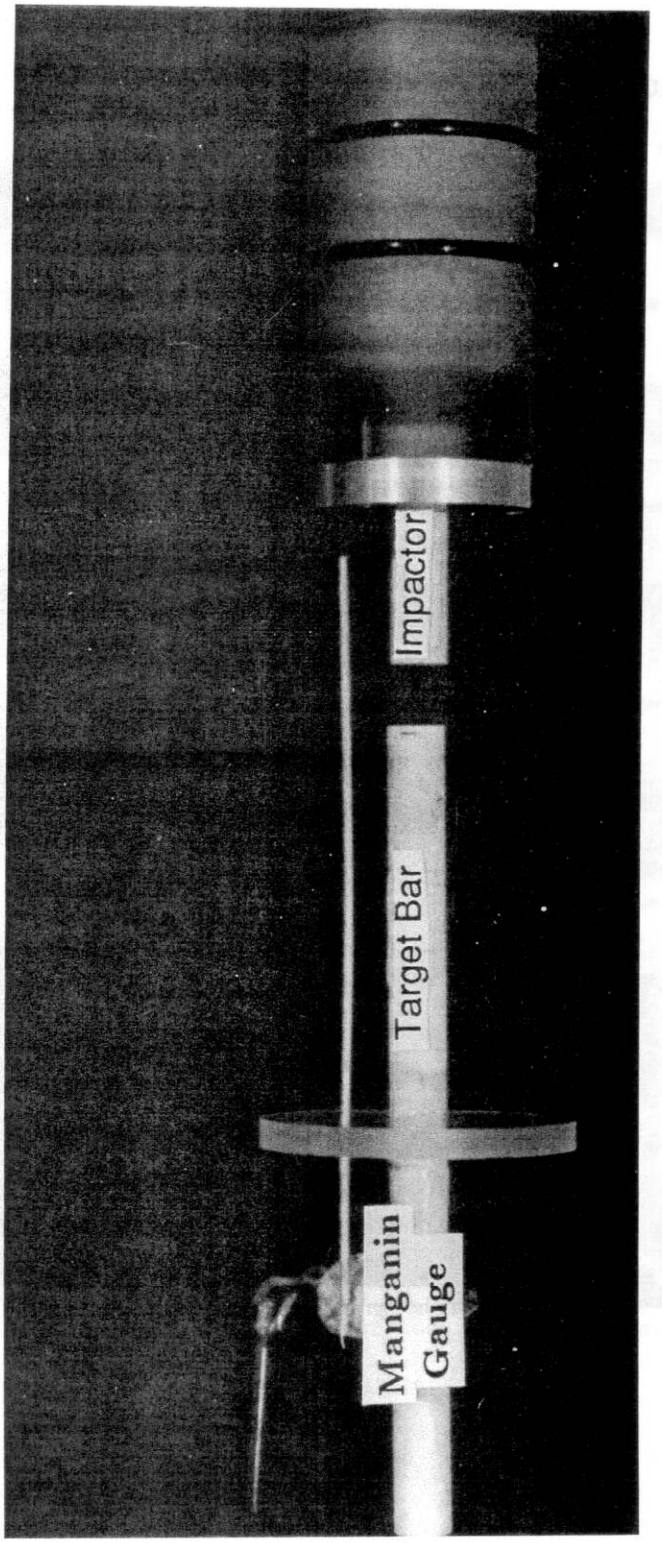

Fig. 1. Experimental configuration.

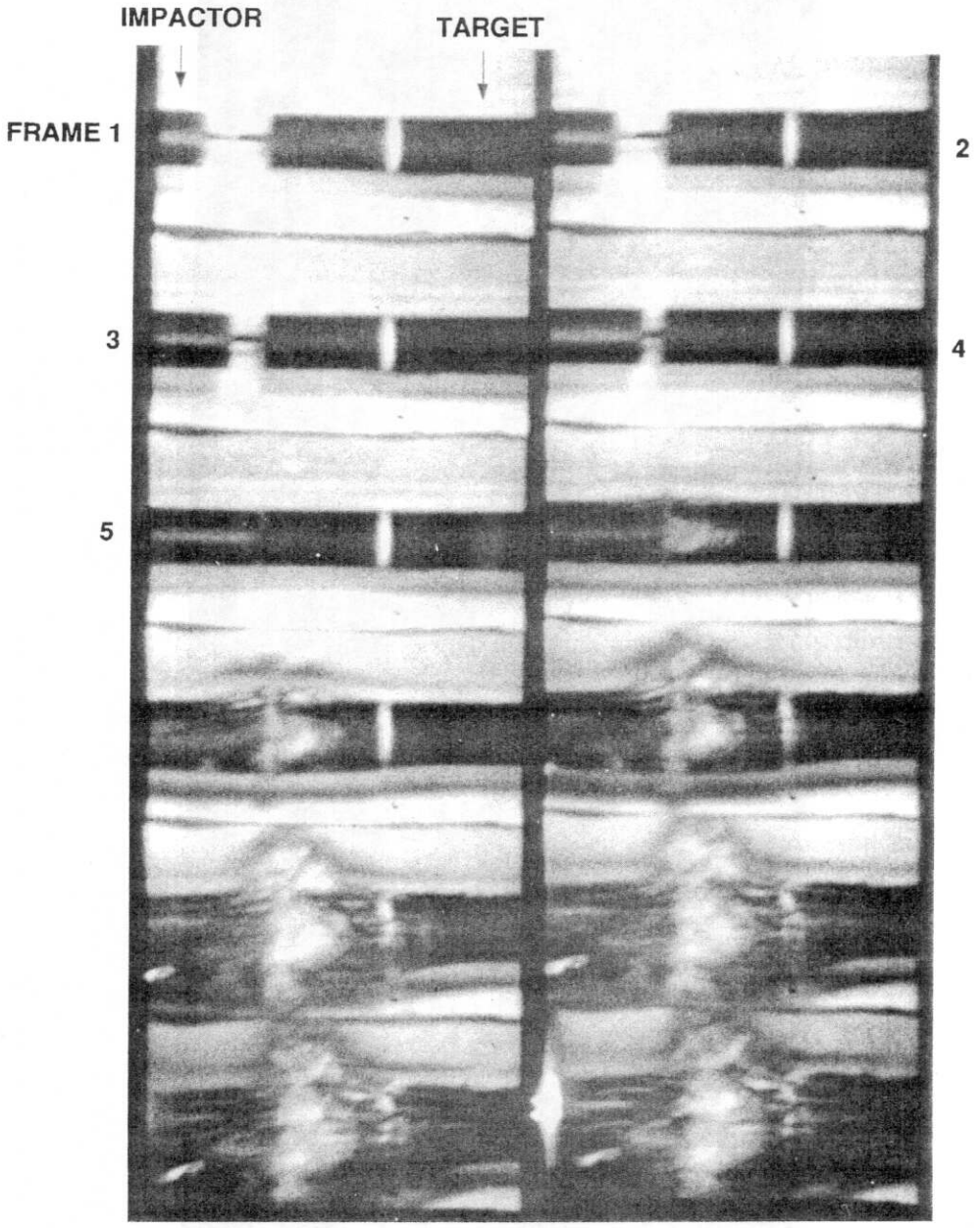

Fig. 3. Sequence of framing camera photographs in experiment 7-1385. Frames are 10 μs apart.

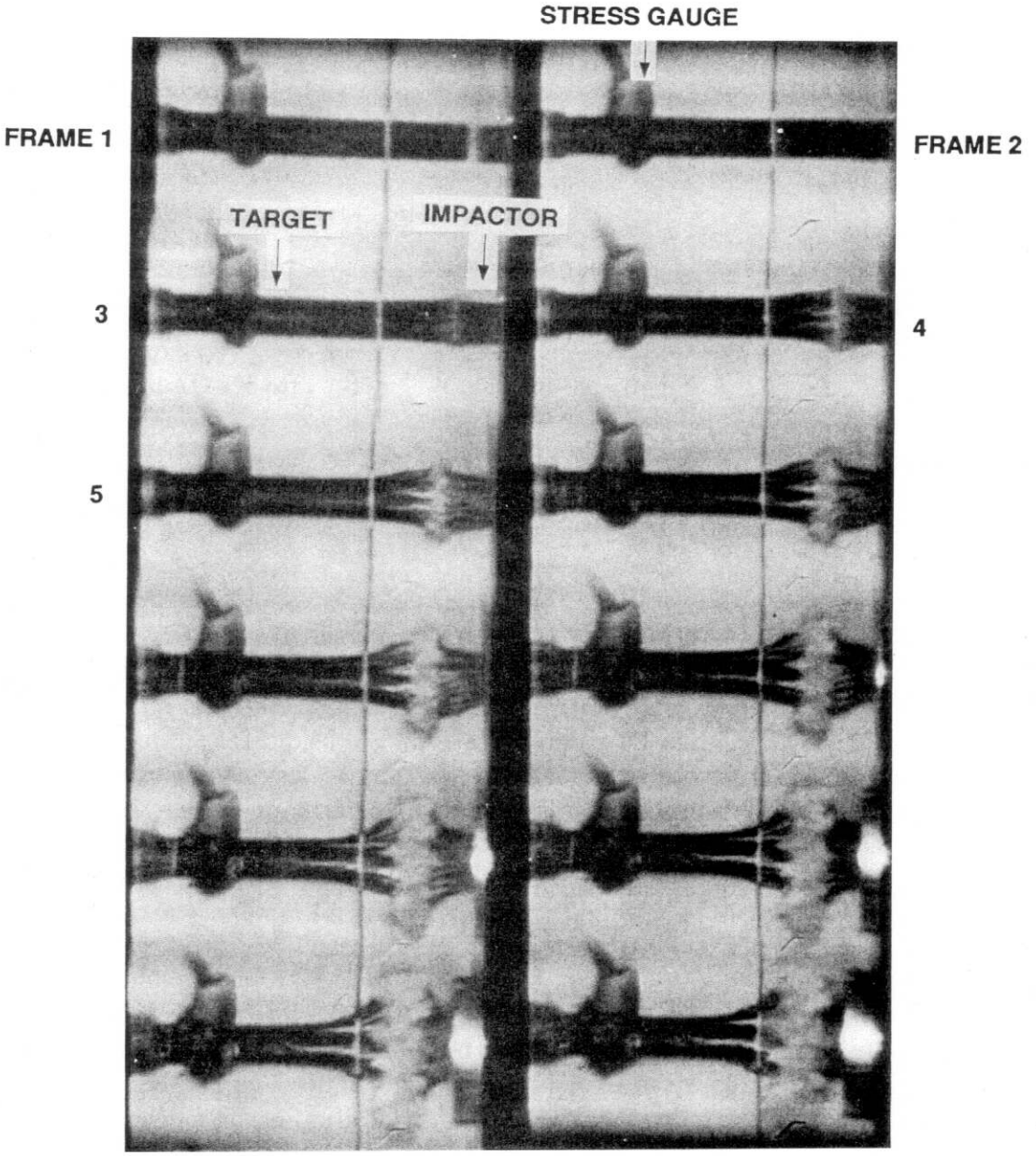

Fig. 4. Sequence of framing camera photographs in experiment 7-1748. Frames are 10 μs apart.

Table 1. *Summary of experimental results*

Shot no.	Impactor type/dim.* (mm)	Imp. vel. (m/s)	Target mat./conf.† (mm)	Tilt (deg)	Pulse width @75% of peak (μs)	Measured stress (GPa)
7-1385	AD-998 Bar $L = 50$, $D = 12.7$	306	AD-998 127-g-50	0 ± 0.5	1.3 ± 0.1	$\sigma_1 = 3.95 \pm 0.1$
7-1389	AD-998 Bar $L = 63.5$, $D = 12.7$	99	AD-998 127-g-50	0 ± 0.5	8.5 ± 0.1	$\sigma_1 = 2.1 \pm 0.1$
7-1331	AD-94 Bar $L = 50$, $D = 12.7$	297	AD-94 127-g-50	0 ± 0.5	1.0 ± 0.1	$\sigma_1 = 2.7 \pm 0.1$
7-1748	Cored AD-995 bar $L = 50.8$, $D = 12.7$	278	Cored AD-995 76-g-25.4	0 ± 0.5	1.3 ± 0.1	$\sigma_1 = 3.5 \pm 0.2$
7-1750	Cored AD-995 bar $L = 50.8$, $D = 12.7$	175	Cored AD-995 76-g-25.4	0 ± 0.5	2.5 ± 0.1	$\sigma_1 = 3.6 \pm 0.3$

* L = length; D = diameter.
† g = gauge.

NC) were embedded at 10 diameters in the AD-998 and AD-94 bars and at 6 diameters away in the cored AD-995 bars from the impact faces. The gauges were backed by 25.4 or 50 mm long pieces of the bars of the same material as the front piece. The back pieces of the assembled bar targets were set in a lexan disk in order to align the target for a planar impact. A coaxial trigger pin was also set through a hole in the lexan ring to trigger a manganin gauge bridge circuit and a high speed Imacon camera. The bars were painted black so that cracks and faults could be distinguished during the failure event.

The impactor bars were 12.7 mm in diameter and were of the same type of alumina bar as that of the target. These were glued in a hole machined in the lexan sabot and the heights above the sabot surface were normally 12.7–28 mm. A total of five experiments was performed using the 50 mm gas/powder gun at the University of Dayton Research Institute. High Speed Imacon camera was operated at 10^5 frames per second. Measured profiles of manganin gauges were converted to stress–time profiles following the calibration by Rosenberg and Partom, 1985.

2.2. *Experimental results*

The experiments discussed in this paper are summarized in Table 1. Impact velocities between 99 and 306 m/s have been used. At 99 m/s (experiment 7-1389) the material remains elastic and the compressive wave duration, of approximately 10 μs, is determined by the arrival of the unloading wave from the free end of the target bar to the gauge location.

The measured stress profiles are given in Fig. 2. It can be observed that the stress level remains high with a peak stress approximately equal to the one predicted by

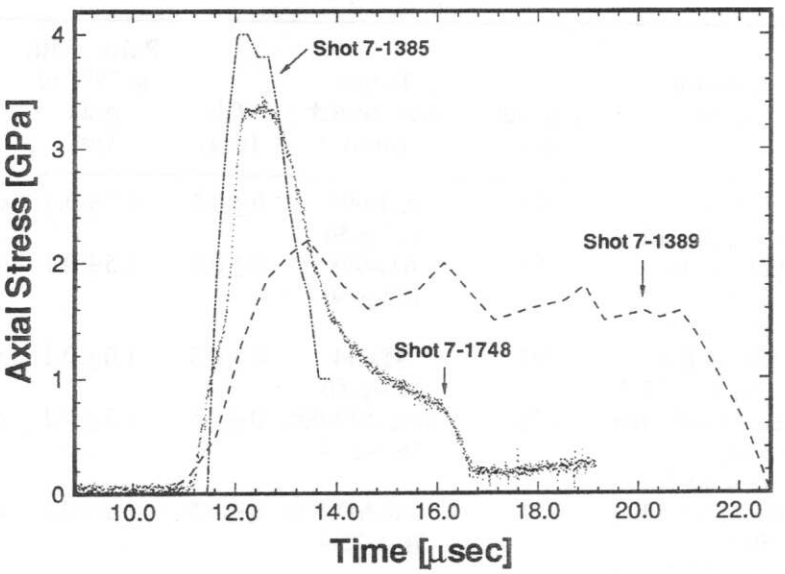

Fig. 2. Measured stress profiles at 127 mm from the impact surface in experiments 7-1389 and 7-1385 and at 76 mm in experiment 7-1748.

elastic one dimensional stress. By contrast, when the impact velocity is high enough to introduce damage, for instance experiments 7-1385 and 7-1748, the maximum compressive stress is sustained for only 200 ns with a main pulse duration of approximately 1.8 μs followed by a tail, see Fig. 2. Furthermore, the measured peak stress is only 70% of the computed peak stress assuming elastic 1-D stress conditions. This indicates the peak stress is attenuated before the wave reaches the gauge location. It should be noted that in this case the pulse duration is controlled by the damage process rather than by unloading from the free end of the target bar.

The evolution of damage can be observed in the sequence of photographs, with each frame every 10 μs, shown in Figs 3 and 4. In the case of experiment 7-1385, Fig. 3, the first frame is shown in the upper left corner; a gap between the target and impactor bars can be noticed to the left of the vertical fiducial mark. Impact takes place sometime between the fourth and fifth frames. In the sixth frame a radial expansion is clearly observed which becomes more evident in the subsequent frames. Well defined patterns of axial cracks are also observed in a region approximately two bar diameters in size, symmetrically formed from the impact surface. A violent radial expansion with a debris of fined particles results from accumulated damage and pulverization of the material. This failure mechanism has been identified in all aluminas independently of the impurity content. A sequence of photographs recorded in experiment 7-1748, Fig. 4, illustrates this feature. As in the case of sintered AD-998 alumina this AD-995 alumina with a larger glass content also fails by bar splitting.

3. MODELING

3.1. *A microcracking multiple-plane model*

In this section the inelastic response of brittle and quasi-brittle materials is modeled through a microcracking multiple-plane model based on a dilute approximation

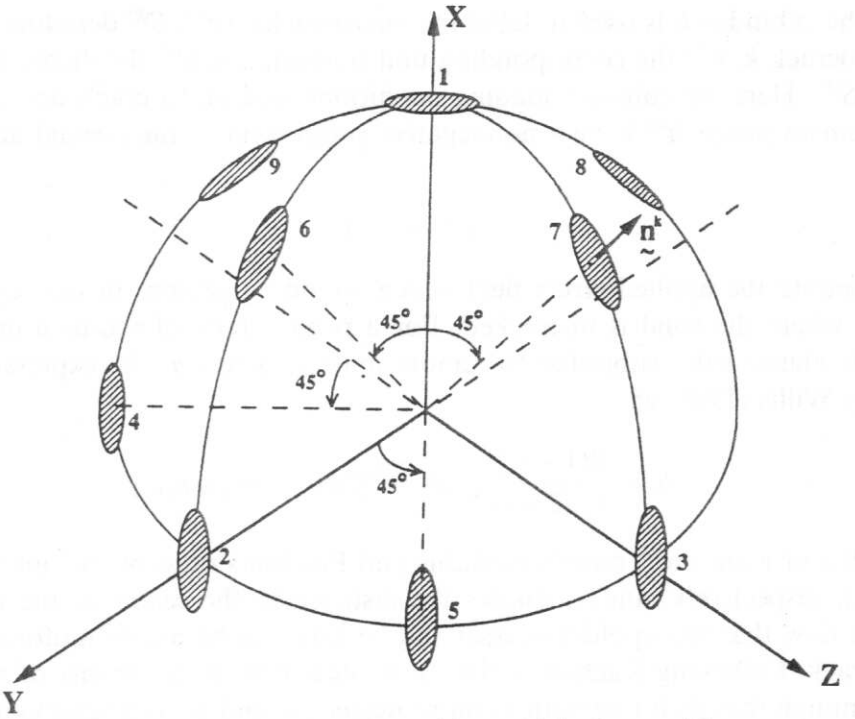

Fig. 5. Schematic of microcracking multiple-plane model.

(Taylor model). Our formulation overlaps with some theories in which multiple-plane representations of inelasticity are derived, e.g. Seaman and Dein (1983), Bazant and Gambarova (1984), Ju and Lee (1991a,b). In the quasi-static case, Ju and Lee (1991a,b), employed a self-consistent method together with an analytical solution for weakly interacting cracks in order to derive inelastic compliances. Unfortunately, the averaging methods used to compute effective moduli do not admit a straightforward extension into the dynamic range.

The basic concept is that microcracking and/or slip can occur on a discrete number of orientations (Fig. 5). In our computational model, the slip plane properties (friction, initial microcrack size, microcrack density, etc.) and their evolution are independently computed on each plane. The macroscopic response of the material is based on an additive decomposition of the strain tensor into an elastic part and an inelastic contribution arising from the presence of microcracks within the solid. In contrast to scalar representations of damage, e.g. Rajendran (1992), the present formulation is broad enough to allow the examination of damage induced anisotropy and damage localization in the interpretation of impact experiments.

3.1.1. *Stress–strain relations in tension.* Consider a representative volume V of an elastic solid containing a large number of microcracks. The average strains contributed by the open microcracks are given by

$$\varepsilon_{ij}^{c} = \frac{1}{V}\sum_{k}\int_{S^{(k)}} \tfrac{1}{2}(b_i^{(k)}n_j^{(k)} + n_i^{(k)}b_j^{(k)})\,\mathrm{d}S \tag{1}$$

where the subindex k is used to label the microcracks, with $S^{(k)}$ denoting the surface of microcrack k, $\mathbf{n}^{(k)}$ the corresponding unit normal, and $\mathbf{b}^{(k)}$ the displacement jump across $S^{(k)}$. Here we consider loading conditions leading to crack opening, i.e. the displacement jumps $\mathbf{b}^{(k)}$ have a nonnegative component in the normal direction $\mathbf{n}^{(k)}$, namely,

$$b_i^{(k)} n_i^{(k)} \geqslant 0. \tag{2}$$

Let $\boldsymbol{\sigma}$ denote the applied stress field which would be present in the representative volume where the solid is uncracked. For a penny crack of radius a in an infinite isotropic elastic solid subjected to remote uniform stress $\boldsymbol{\sigma}$, the expression for $\mathbf{b}$ is given by Willis (1968) as

$$b_i = \frac{8(1-\nu^2)}{\pi E(2-\nu)} \sqrt{a^2 - r^2}\,[2\sigma_{ij} n_j - \nu \sigma_{jk} n_j n_k n_i] \tag{3}$$

where E and ν are the Young's modulus and Poisson's ratio of the uncracked solid (matrix), respectively, and r denotes the distance to the center of the microcrack. Assume now that the applied stresses can be taken to be nearly uniform over each microcrack. Following Kachanov (1980), we note that, if the density of microcracks is low enough that their interaction can be neglected, and all microcracks are assumed to be planar, then

$$\varepsilon_{ij}^c = \frac{1}{V} \sum_k S^{(k)} \tfrac{1}{2} (\bar{b}_i^{(k)} n_j^{(k)} + n_i^{(k)} \bar{b}_j^{(k)}) \tag{4}$$

where

$$\bar{b}_i^{(k)} = \frac{1}{S^{(k)}} \int_{S^{(k)}} b_i^{(k)}\, \mathrm{d}S = \frac{16(1-\nu^2)}{3E(2-\nu)} a^{(k)} (2\sigma_{ij} n_j^{(k)} - \nu \sigma_{jl} n_j^{(k)} n_l^{(k)} n_i^{(k)}) \tag{5}$$

is the average displacement jump across microcrack k.

Within the framework of a multiple-plane model with nine independent orientations of microcracks (see Fig. 5), the inelastic strain tensor is given by

$$\varepsilon_{ij}^c = \sum_{k=1}^{9} N^{(k)} S^{(k)} \tfrac{1}{2} (\bar{b}_i^{(k)} n_j^{(k)} + n_i^{(k)} \bar{b}_j^{(k)}) \tag{6}$$

in which $N^{(k)}$ is the microcrack density of each orientation. In the present formulation, $N^{(k)}$ is assumed constant, although an initial distribution as a function of stress and an evolution equation could be proposed, Seaman *et al.* (1978). At the present time information on $N^{(k)}$ and its evolution are not available for the material under investigation. Development of recovery experiments, which will allow the post-test examination of the samples, is needed.

3.1.2. *Stress–strain relations in compression.* The point of departure is again (6) which gives the average inelastic strain, due to microcracking, of a representative volume of material. Because the inequality (2) is not satisfied in this case, the effective shear traction can be defined as

$$f_i = (\tau + \mu\sigma_n)(\mathbf{n}_\tau)_i, \tag{7}$$

in which μ is the friction coefficient of the microcrack faces, τ and σ_n are the resolved shear stress and the normal stress acting on the microcrack, respectively, and $\mathbf{n}_\tau$ is the unit vector in the direction of the resolved shear traction. Throughout this section the superindex k is implicit.

The average sliding of the faces of the crack, following from Willis' (1968) result (3), is

$$\bar{b}_i = \frac{32(1-\nu^2)}{3\pi E(2-\nu)} a f_i. \tag{8}$$

Embodied in (8) is the notion that $\mathbf{f}$ provides the effective driving force for the sliding of the microcracks. A revealing alternative form of (8) may be derived as follows. Let $\bar{b} = |\bar{\mathbf{b}}|$ be the magnitude of the sliding displacement. Then, multiplying (8) by $\mathbf{t}$ and after some rearrangement, one finds that the relation

$$\phi(\sigma_n, \tau, \bar{b}) \equiv \tau + \mu\sigma_n - \frac{3\pi E(2-\nu)}{32(1-\nu^2)a}\bar{b} = 0 \tag{9}$$

must be identically satisfied during sliding. Equation (9) may be regarded as a balance of forces: the first term τ represents the externally applied driving force; the second, $\mu\sigma_n$, the frictional resistance; and the third, the restoring force from the surrounding elastic medium. When sliding occurs, the friction condition (9) together with the equation of evolution for a determine the evolution of $\bar{b}$.

3.1.3. *Dynamic microcrack growth.* In order to compute the inelastic strain tensor at all times, it becomes necessary to follow the evolution of the microcrack radius $a(\mathbf{n})$ in the selected orientations. The structure of this equation is obtained by means of the following argument. Assume that microcrack growth is governed by a dynamic toughness, $K_d(\dot{a})$, which depends on the crack tip velocity, i.e. growth is sustained provided that

$$K(a, \dot{a}; t) = K_d(\dot{a}), \tag{10}$$

where K is an effective dynamic stress intensity factor on the microcrack front. For a given loading, K may be expected to be a function of the current crack size a, the velocity of the crack tip $\dot{a}$, and the time t, through the temporal dependence of the loading (Freund, 1990).

It is shown in Espinosa (1994) that in the case of mixed mode loading the equation of evolution for $\dot{a}$ is

$$\dot{a} = mc_R[1-(K_{IC}/K_{eff})^n] \geqslant 0, \tag{11}$$

where n and m are phenomenological material constants which may have different values in tension and compression, and K_{eff} is an effective stress intensity factor. For mixed mode conditions, K_{eff} is derived by considering an average energy release rate associated with an increase in radius of the microcracks, namely,

$$\mathscr{G} = \frac{1}{2\pi}\int_0^{2\pi} \frac{1-\nu^2}{E}[K_{\mathrm{I}}^2 + K_{\mathrm{II}}^2 + K_{\mathrm{III}}^2/(1-\nu)]\,\mathrm{d}\theta \tag{12}$$

and,

$$K_{\mathrm{eff}} = \sqrt{\frac{\mathscr{G}E}{1-\nu^2}}. \tag{13}$$

3.2. *Numerical implementation*

The general structure of the constitutive equations corresponds to that of a solid with a damage induced anisotropic stress–strain relation with elastic degradation. In particular, the effective behavior of the solid is predicted to be rate dependent due to crack kinetics effects. From a computational standpoint, this ensures numerical reliability and mesh independence (Needleman, 1988; Espinosa, 1989). This is in contrast to quasi-static formulations of damage for which the governing equations become ill-posed in the softening regime (Sandler and Wright, 1984). If the material is subjected to a predominantly tensile stress state, microcracks along orientations perpendicular to the direction of maximum tensile stresses will grow according to (11). In this case, significant dilation is expected due to mode I crack opening. If a predominantly compressive state of stress with shear is imposed, then crack opening is inhibited but inelasticity is manifested by the growth of penny-shaped cracks in modes II and III (shear modes).

Based on an additive decomposition of the strain tensor, and assuming Hooke's law, the equations governing the response of the material are

$$\sum_{k=1}^{9} \tfrac{1}{2}N^k S^k(\bar{\mathbf{b}}^k\mathbf{n}^k + \mathbf{n}^k\bar{\mathbf{b}}^k) = \boldsymbol{\varepsilon} - \left(\frac{1+\nu}{E}\boldsymbol{\sigma} - \frac{\nu}{E}\sigma_{kk}\mathbf{I}\right). \tag{14}$$

The expression for $\mathbf{b}^k$ is a function of the loading mode on each plane as previously discussed. For simplicity, only the equations corresponding to the compressive mode will be given in detail. A similar treatment applies to the other cases.

Substitution of (8) into (14) gives the following stress–strain relations:

$$\sum_{k=1}^{9} \frac{16(1-\nu^2)}{3E(2-\nu)}(a^k)^3 N^k[(\boldsymbol{\sigma}\cdot\mathbf{n}^k)\mathbf{n}^k + \mathbf{n}^k(\boldsymbol{\sigma}\cdot\mathbf{n}^k) - (\mathbf{n}^k\cdot\boldsymbol{\sigma}\cdot\mathbf{n}^k)(2\mathbf{n}^k\mathbf{n}^k - \mu(\mathbf{n}_\tau)^k\mathbf{n}^k$$
$$- \mu\mathbf{n}^k(\mathbf{n}_\tau)^k)] = \boldsymbol{\varepsilon} - \left[\frac{1+\nu}{E}\boldsymbol{\sigma} - \frac{\nu}{E}\sigma_{kk}\mathbf{I}\right]. \tag{15}$$

Differentiation of (15) with respect to time provides the constitutive equations in rate form. Fully implicit integration of this equation is computationally too intensive, while explicit integration lacks accuracy and becomes unstable during unloading when substantial damage within the material has developed. These disadvantages are overcome through the use of a semi-implicit scheme in which the crack-tip equation of motion, and the direction of the shear traction on the microcrack plane are explicitly

updated, while the remaining variables are treated implicitly. Under these conditions, the relation between the stress rate tensor and the total strain rate tensor becomes

$$\left(\frac{1+\nu}{E}\dot{\boldsymbol{\sigma}}-\frac{\nu}{E}\dot{\sigma}_{kk}\mathbf{I}\right)+\sum_{k=1}^{9}\frac{16(1-\nu^2)}{3E(2-\nu)}N^k((a^k)^3+3(a^k)^2\dot{a}^k\Delta t)[(\dot{\boldsymbol{\sigma}}\cdot\mathbf{n}^k)\mathbf{n}^k+\mathbf{n}^k(\dot{\boldsymbol{\sigma}}\cdot\mathbf{n}^k)$$

$$-(\mathbf{n}^k\cdot\dot{\boldsymbol{\sigma}}\cdot\mathbf{n}^k)(2\mathbf{n}^k\mathbf{n}^k-\mu(\mathbf{n}_\tau)^k\mathbf{n}^k-\mu\mathbf{n}^k(\mathbf{n}_\tau)^k]_{i+1}$$

$$+\sum_{k=1}^{9}\frac{16(1-\nu^2)}{3E(2-\nu)}N^k(a^k)^3\mu(\mathbf{n}^k\cdot\dot{\boldsymbol{\sigma}}\cdot\mathbf{n}^k)_{i+1}[(\mathbf{n}^k\dot{\mathbf{n}}_\tau^k+\dot{\mathbf{n}}_\tau^k\mathbf{n}^k)]\Delta t$$

$$=\dot{\boldsymbol{\varepsilon}}_{i+1}-\sum_{k=1}^{9}\frac{16(1-\nu^2)}{3E(2-\nu)}N^k3(a^k)^2\dot{a}^k[(\boldsymbol{\sigma}\cdot\mathbf{n}^k)\mathbf{n}^k+\mathbf{n}^k(\boldsymbol{\sigma}\cdot\mathbf{n}^k)-(\mathbf{n}^k\cdot\boldsymbol{\sigma}\cdot\mathbf{n}^k)(2\mathbf{n}^k\mathbf{n}^k$$

$$-\mu(\mathbf{n}_\tau)^k\mathbf{n}^k-\mu\mathbf{n}^k(\mathbf{n}_\tau)^k]_i-\sum_{k=1}^{9}\frac{16(1-\nu^2)}{3E(2-\nu)}N^k(a^k)^3\mu(\mathbf{n}^k\cdot\boldsymbol{\sigma}\cdot\mathbf{n}^k)_i[(\mathbf{n}^k\dot{\mathbf{n}}_\tau^k+\dot{\mathbf{n}}_\tau^k\mathbf{n}^k)],\quad(16)$$

in which the indices i and $i+1$ refer to two subsequent times. This equation corresponds to the case in which the effective shear traction on the surface of the crack is such that additional slipping occurs, i.e. $\mathbf{b}^k>0$. Similar expressions can be derived for the sticking case, in which (9) is satisfied with $\dot{\mathbf{b}}^k=0$. Equation (16) can be written in matrix form and the stress rate tensor obtained by simple elimination. After the stress rate tensor is known, the average displacement jump rates and inelastic strain rates can be computed from the following equations:

$$\dot{\bar{\mathbf{b}}}^k=\frac{32(1-\nu^2)}{3\pi E(2-\nu)}[a^k(|\dot{\tau}|^k+\mu\dot{\sigma}_n^k)\mathbf{n}_\tau^k+\dot{a}^k(|\tau|^k+\mu\sigma_n^k)\mathbf{n}_\tau^k+a^k(|\tau|^k+\mu\sigma_n^k)\dot{\mathbf{n}}_\tau^k],\quad(17)$$

$$\dot{\boldsymbol{\varepsilon}}^c=\sum_{k=1}^{9}N^k[\pi a^k\dot{a}^k(\bar{\mathbf{b}}^k\mathbf{n}^k+\mathbf{n}^k\bar{\mathbf{b}}^k)+\frac{S^k}{2}(\dot{\bar{\mathbf{b}}}^k\mathbf{n}^k+\mathbf{n}^k\dot{\bar{\mathbf{b}}}^k)].\quad(18)$$

4. NUMERICAL SIMULATIONS

The microcracking multiple-plane model has been utilized in the interpretation of the bar experiments conducted on Al_2O_3 rods. A dynamic finite element axisymmetric analysis is performed to simulate the experiments reported in Section 2. The software used in the calculations is a modified version of FEAP (see Zienkiewicz and Taylor, 1989). The impactor and target bars have a diameter of 12.7 mm, and a length of 80 and 170 mm, respectively. A uniform mesh with four-node quadrilateral elements is used. The element size in the direction of wave propagation is 0.5 mm. Symmetry boundary conditions are imposed at the bar axis. In order to preserve axisymmetric conditions, only planes 1, 2, 6 and 8 are included in the analysis (see Fig. 5). The model parameters used in the calculations are $N=1\times10^{12}/\mathrm{m}^3$ for planes 1 and 2, $N=1\times10^{10}/\mathrm{m}^3$ for planes 6 and 8, $K_{IC}=1.7\,\mathrm{MPa}\sqrt{m}$, $\mu=0.1$, $a_0=1\ \mu\mathrm{m}$, $n^+=m^+=0.3$, and $n^-=m^-=0.1$. Whenever different parameters are used, the corresponding plots indicate the variation with respect to these values.

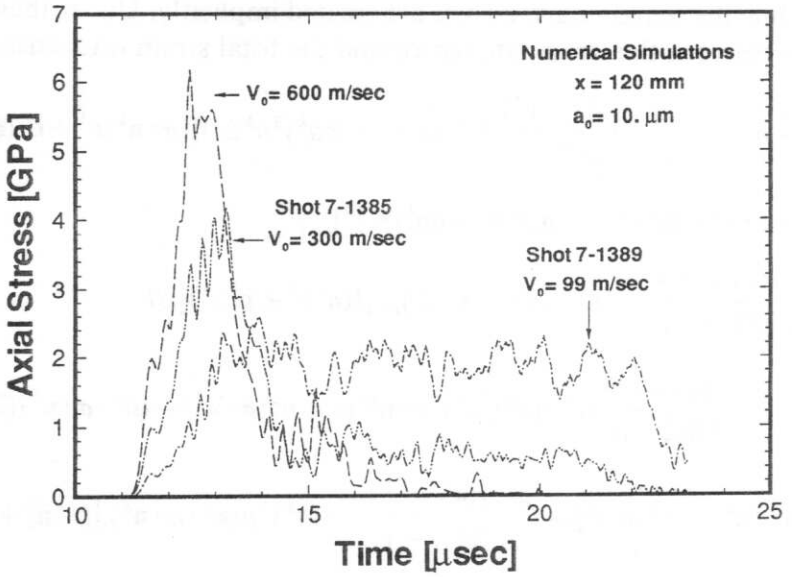

Fig. 6. Computed axial stress histories for 99, 300 and 600 m/s impact velocities.

The model parameters are selected such that a damage threshold is properly captured and at the same time they are in agreement with values reported in the literature. Microstructural differences have an effect on model parameters. For instance, the existence of a second phase at the grain boundaries controls parameters μ, $n^{\pm}$, $m^{\pm}$ and K_{IC}. The grain size controls the values of a_0 and maximum density of each orientation. The choice of different crack densities as a function of orientation is motivated by experimental data (Espinosa *et al.*, 1992) indicating that the density of active microcracks is a function of the mechanism responsible for crack nucleation. In the case of predominantly compressive stress states, glass at the grain boundaries determines the early stages of inelasticity and acts as a precursor for the development of triple point microcracks. In the case of predominantly tensile stress states, cracks are mainly nucleated due to grain boundary decohesion at a much lower stress level. In the present calculations, plane 1 is a plane on which positive normal tractions result from unloading waves emanating from the bar surface. By contrast planes 6 and 8 are mainly shear cracks.

The effect of impact velocity on the stress histories is shown in Fig. 6. The microcracking model with the above parameters has been utilized. The simulations capture the long pulse duration in the case of shot 7-1389 (impact velocity 99 m/s) basically because the material remains undamaged. A peak stress of approximately 2 GPa is predicted with oscillations introduced by radial release waves originated at the bar surface.

A different situation is observed in the case of experiment 7-1385, in which an impact velocity of 300 m/s was used. After the stress pulse reaches a peak stress of 4 GPa, the axial stress is rapidly attenuated leading to a main pulse duration of only 4.5 μs. When the impact velocity is increased to 600 m/s, a peak stress of 6 GPa is predicted. This higher peak stress is the result of the model rate sensitivity due to crack kinetics effects. A slightly higher stress attenuation rate and a shorter pulse duration are also observed.

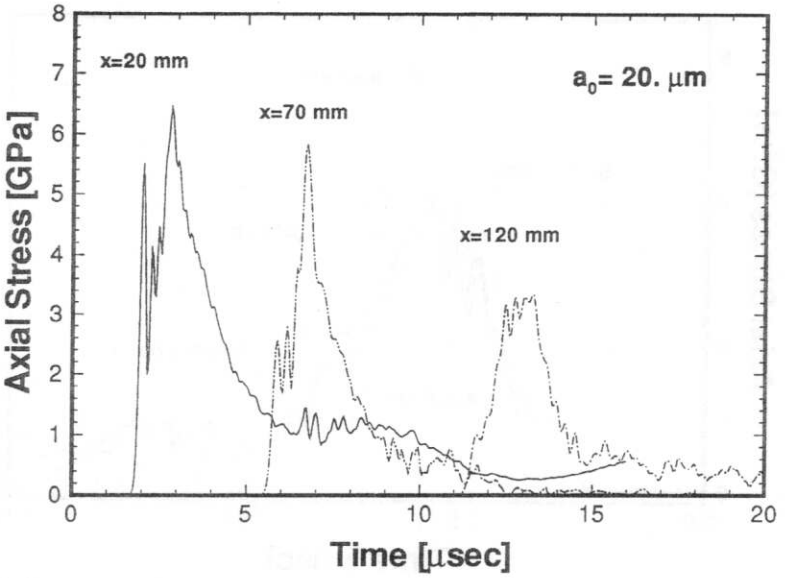

Fig. 7. Computed axial stress histories at 20, 70 and 120 mm from the impact surface.

In both cases the rising part of the stress profile shows features characteristic of wave propagation in rods. A cusp in the stress history corresponding to the separation between a first compressive wave, traveling under uniaxial strain conditions (acoustic wave speed), and a second compressive wave corresponding to the arrival of a longitudinal wave, traveling under uniaxial stress conditions (bar wave speed), is observed. During these early times the material response is basically elastic.

Some additional aspects of the wave propagation event can be observed in Fig. 7, in which the axial stress histories have been plotted at three locations along the ceramic rod. The configuration and impact velocity of shot 7-1385 is used, but no comparison is made because only one stress history is recorded experimentally. A strong stress attenuation at the wave front occurs due to waveguide effects. The formation of the second compressive wave with a very well defined structure is recorded at 120 mm from the impact surface. This wave also presents a significant peak stress reduction when an initial microcrack radius of 20 μm is used.

Almost no attenuation occurs when the initial microcrack radius is set to 1 μm, see Fig. 8. A comparison between the numerical simulations and two experimental records (7-1385 and 7-1748) is performed in the same figure. Agreement with the experimentally measured stress–time profile, using manganin gauges, is achieved with $a_0 = 10$ μm. Peak stress and pulse duration are well characterized by the model. It is also seen that for large values of a_0 a long tail develops, due to wave dispersion, in agreement with the recorded stress history in experiment 7-1748. In experiment 7-1385, the embedded manganin gauge failed after approximately 2 μs and therefore the tail has not been observed. Some of the oscillations present in the numerical simulations may be related to a limited spatial resolution of the mesh. A run performed with a finer mesh presents a smoother velocity history but the relevant features were unchanged.

The fact that a large value of a_0 is required to match the experimental records deserves further analysis. From a micromechanical standpoint, the existence of an

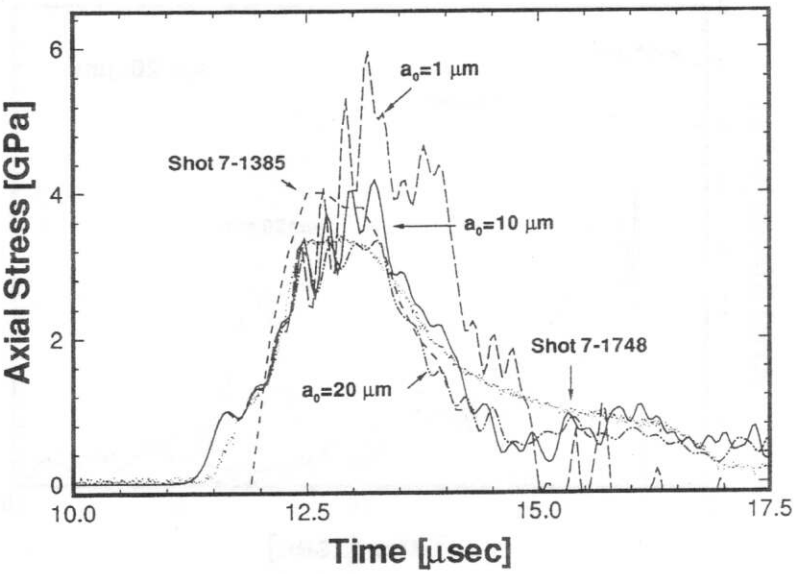

Fig. 8. Comparison of numerical simulations and experimental record for experiment 7-1385. The stress history recorded in experiment 7-1748 is also plotted to show wave dispersion effects.

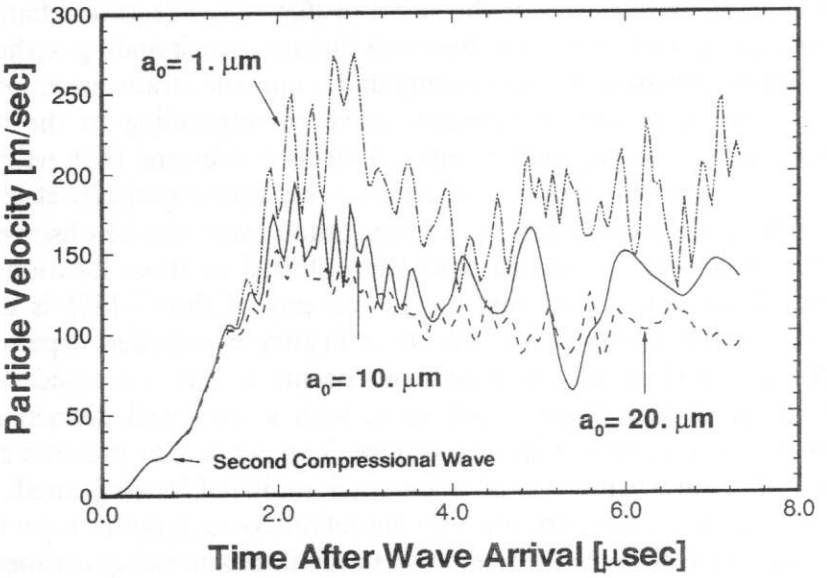

Fig. 9. Axial velocity histories at the target bar free end for three different initial microcrack radii.

initial microcrack radius implies the generation of a nonzero inelastic strain rate at the wave front. The net effect is an elastic precursor attenuation proportional to a_0^3. The need for a significant value of a_0 to achieve the best fitting of the experimental records can be linked to the presence of a glassy phase in the tested aluminas. Espinosa *et al.* (1992) have shown that the onset of inelasticity in aluminas containing a glassy phase is controlled by the shear resistance of this phase which leads to grain boundary shearing and a plastic-like behavior. Furthermore, this shearing leads to triple point microcracks that can grow further under the applied loading.

Further evidence of the compressive wave attenuation can be seen in a plot of axial particle velocity at the rod end as a function of initial microcrack radius, see Fig. 9.

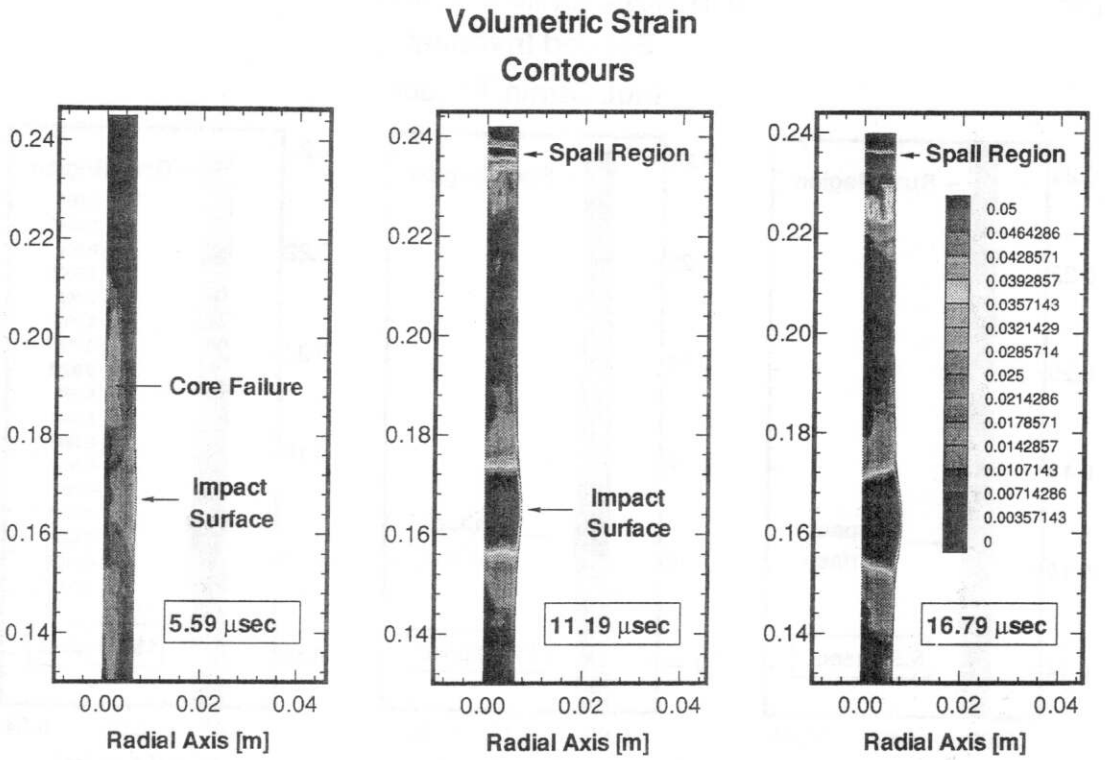

Fig. 10. Contours of volumetric strains, in the deformed configuration, at three different times after impact.

The double wave structure is again noticeable in all traces, although the ramping slope of the second compressional wave is different. It can be appreciated that the particle velocity reaches an almost constant magnitude in the first 3.5 μs followed by a decay and subsequent increase to a lower relatively constant amplitude. This pull back signal can be correlated to bar spalling upon reflection of the compressive pulse as explained in the next paragraph. The particle velocity histories replicate the features observed in interferometrically measured axial velocities (Grady and Wise, 1993), in particular when a large a_0 is utilized. These calculations clearly show that the free surface particle velocity level is controlled by the strength of the compressive pulse reaching the free end of the bar.

In view of the experimentally measured and computed stress pulses, in which a short pulse duration is observed, the constancy of the free surface particle velocity for long periods of time needs clarification. Contours of volumetric strains in the discretized field at three different times are given in Fig. 10. It should be noted that volumetric strains larger than zero correspond to tensile damage, crack opening, which in this case is confined to the central region of the bar. At 11.19 μs a well defined spall region develops in the impactor bar, as a result of the shape and duration of the compressive wave reaching the bar free surface. A similar dynamic tensile failure is predicted in the longer target bar, which explains the constancy of the free surface particle velocity mentioned above. Significant amounts of dilation are also observed at the bar core due to tensile fracture of the material. This failure mode is induced by the focusing of release waves from the bar surface.

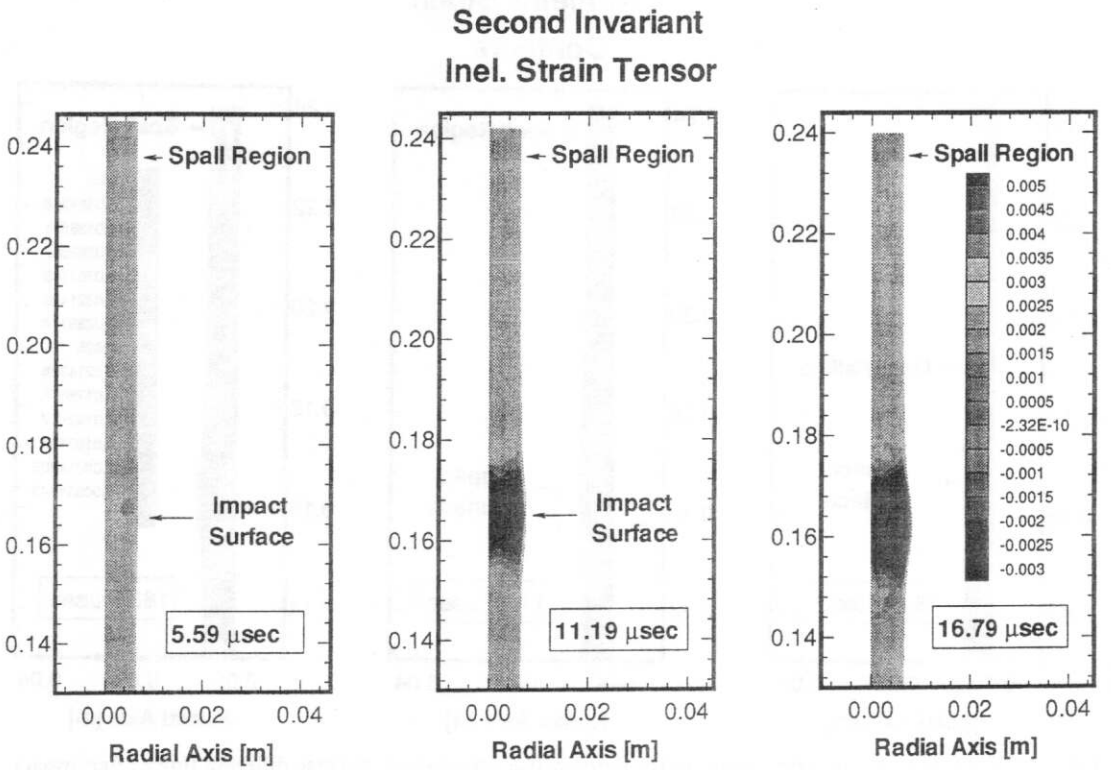

Fig. 11. Contours of the second invariant of the inelastic strain tensor at three different times after impact.

On the basis of these contours one can infer that the bar lateral expansion has two contributions, one from the deformation of the material due to crack growth and shearing under local compressive fields and another from dilation at the core of the bar. The evolution of compressive damage within the bar can be identified by plotting contours of the second invariant of the inelastic strain tensor at different times, Fig. 11. As in the case of volumetric strains, the contours are plotted in the deformed configuration. The numerical simulation predicts extensive compressive damage in a region of approximately one bar diameter in agreement with photographs obtained during the impact event, see Section 2. From this figure it can be seen that the compressive damage gradually extends towards the interior of the bars leading to a significant increase in bar diameter in a region close to the impact surface. If comparison between the high speed photographs and the numerically predicted radial displacements is performed within the first 15 μs, good agreement is observed. It should be noted that the end of the numerical calculation falls between frames 3 and 4 in Fig. 4. Further insight into the deformation mechanisms leading to the increase in bar diameter can be gained by examining crack radius histories of all active orientations, see Fig. 12. The crack radius histories correspond to an element located at the bar core 20 mm from the impact surface. The first cracks to grow are those on orientations 6 and 8, i.e. cracks at $\pm 45^\circ$ with respect to the bar axis. At approximately 2.5 μs splitting cracks (orientation 1) start to grow due to tensile stresses produced by unloading waves generated at the bar periphery. It can be observed that cracks at $\pm 45^\circ$ with respect to the bar axis have a lower rate of growth than cracks parallel to the

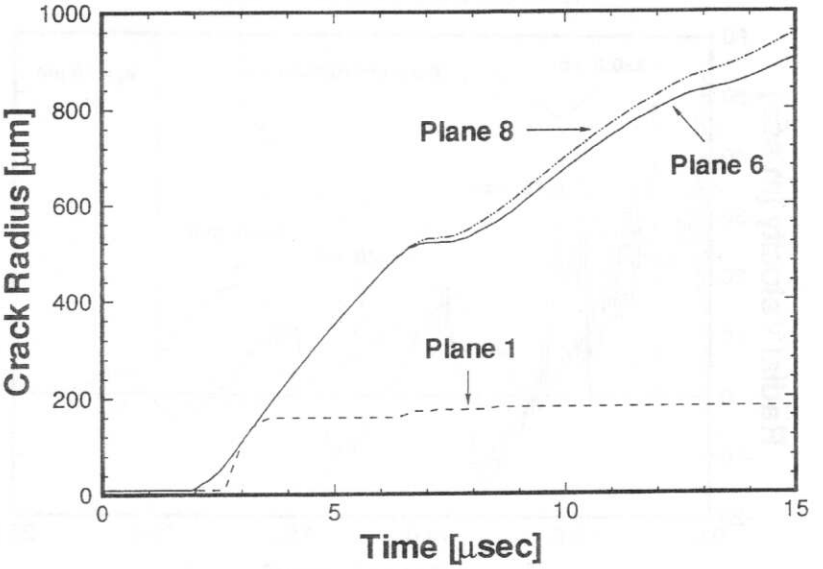

Fig. 12. Crack radius histories of all active orientations for an element at the bar core 20 mm from the impact surface.

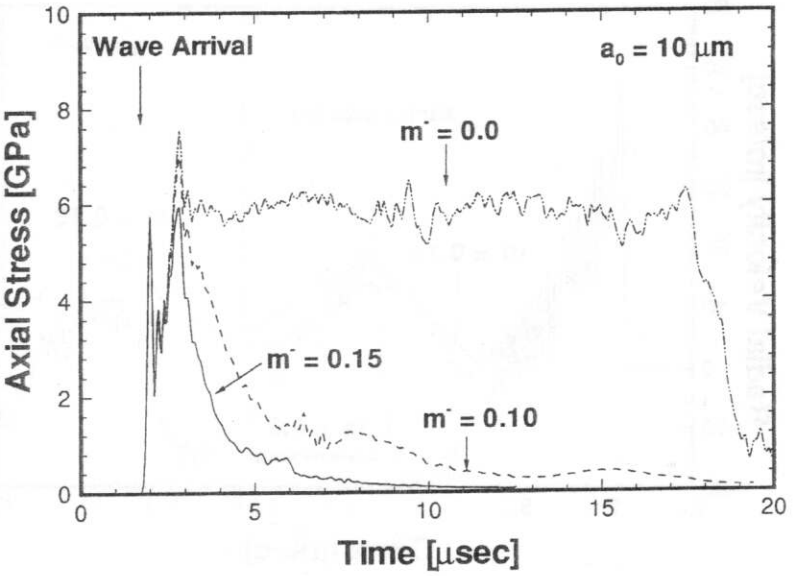

Fig. 13. Axial stress histories at 20 mm from impact surface for three different compressive damage rates.

bar axis (orientation 1). Moreover, cracks perpendicular to the bar axis (orientation 2) exhibit no growth at this location.

Next we examine the effect of compressive damage and its rate on the axial stress histories, see Fig. 13. The axial stress is plotted at a point on the bar axis 20 mm from the impact surface. The tensile damage parameters are the same in all three cases, while different values of m^- have been used. A value of $m^- = 0$ implies no compressive damage. These stress histories clearly show compressive damage and not tensile damage is the feature responsible for the observed stress decay and short pulse durations. Moreover, it can be seen that during the first microsecond the response of

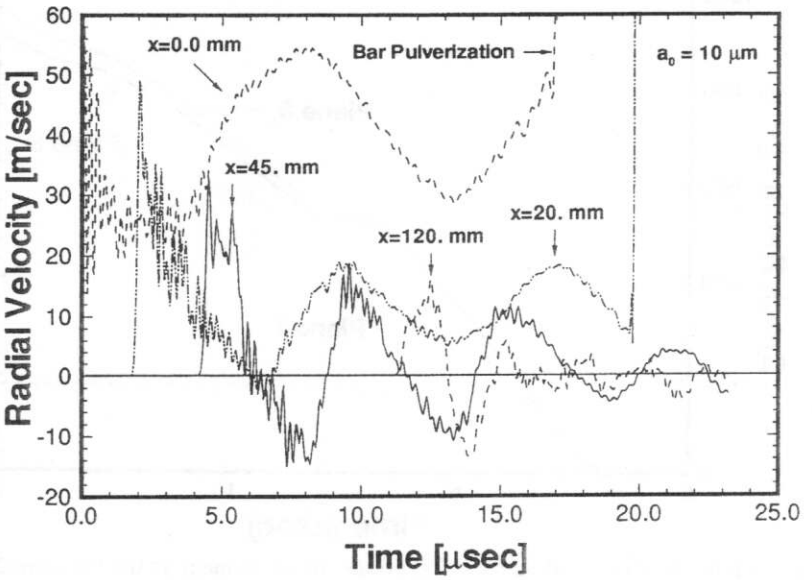

Fig. 14. Plot of radial velocity history variations with distance from the impact surface.

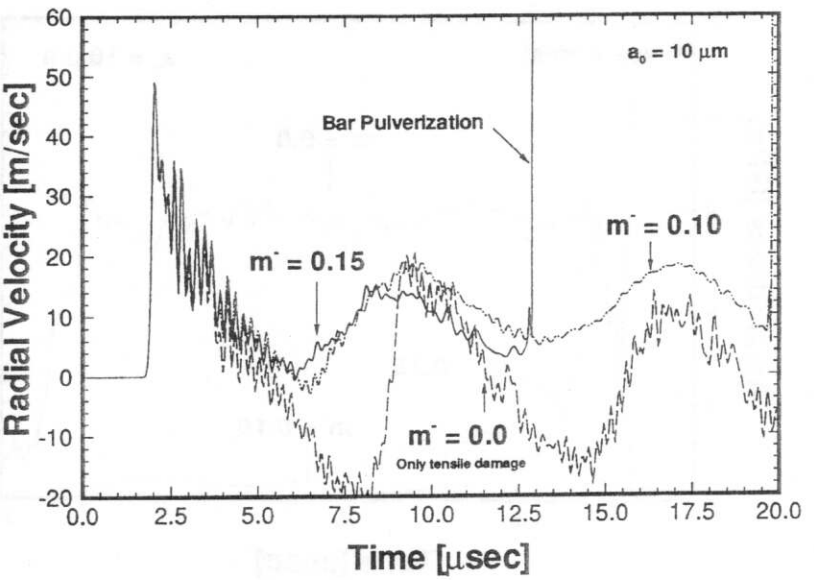

Fig. 15. Radial velocity histories for three values of the parameter m^-.

the material is basically elastic with stress variations dictated by the arrival of release waves from the rod surface. A progressive stress reduction follows with a rate of stress decay controlled by the rate of crack growth (parameter m^- in the model).

In the case of no compressive damage, the axial stress remains approximately constant with a value of 6 GPa, which coincides with computed stress level assuming elastic response. Further information on the effect of damage evolution in the field variables can be obtained from a plot of radial velocities at points located on the bar surface, see Figs 14 and 15. Points located farther away from the impact surface show longer arrival times. In Fig. 14 the variation of the radial velocity with distance from the impact surface is shown. The radial velocity initially jumps to a first peak, reduces

its magnitude and then rises again. This oscillatory structure is preserved at later times although significantly attenuated due to tensile and compressive damage. These velocity variations are produced by radial release waves reverberating within the bar. The strong changes recorded in the first 2.0 μs indicate the initial response of the bar is basically elastic with a progressive increase in inelasticity.

It can be seen that material particles close to the impact plane undergo a significant radial expansion while points farther away show a more moderate expansion. It can be argued that the main difference is related to the failure modes and their distribution along the rod. We have shown earlier that the main compressive damage extends only one diameter from the impact surface while the tensile damage occurs along the bar core and at the end of the bars (spall regions). Therefore, the radial motion of particles close to the impact plane is controlled by compressive damage and its rate, while the radial motion of points farther away is controlled by tensile damage occurring at the bar core.

In Fig. 15 the effect of crack growth rate is illustrated. In the case of pure tensile damage, $m^- = 0.0$, the radial velocity shows an initial variation consistent with an elastic material response followed by an oscillatory radial velocity with regions of negative velocity. By contrast, when compressive damage occurs, the radial expansion becomes larger. It is interesting to note that a large accumulation of damage leads to dramatic increases in radial velocity. If these increases are the consequence of numerical instabilities and/or an indication of material pulverization needs further investigation. Another feature that can be observed in Fig. 15 is the radial velocity oscillations produced by radial release waves. This effect is strongly attenuated in time when compressive damage occurs, $m^- = 0.10$ and 0.15, leading to a smoother radial velocity history.

5. CONCLUDING REMARKS

In this work, we have presented a parametric study of damage and inelasticity on the overall failure of ceramic bars which cannot quantitatively be researched by experiments alone. The simulations allow the decoupling of the relevance of compressive and tensile damage in experimentally recorded stress and velocity histories. Furthermore, the importance of the presence of second phases in the dynamic yield strength and its dependence on propagation distance has been assessed.

The bar impact experiment is a useful technique to study failure in brittle materials. It provides a direct measurement for the yield stress at rates of 10^3–10^4/s. However, in view of the present calculations and experiments, in which the peak of the second compressive stress is highly dependent on distance of propagation, caution must be exercised in its determination. Target rods at least 10 diameters in length may be required especially in the case of ceramics containing second phases at grain boundaries, i.e. Al_2O_3, TiB_2.

Although the unconfined bar experiment subjects the material to large inelastic deformations, at least in a region close to the impact surface, the number of active inelastic planes is smaller than those observed in pressure–shear experiments (Espi-

nosa, 1994). Consequently, the bar experiments should be considered a complementary technique for the characterization of failure mechanisms in brittle materials.

The measured waveforms appear very useful in the examination of constitutive models and numerical solution schemes. In-material stress measurements, with embedded manganin gauges, are very useful in providing axial stress histories that otherwise cannot be obtained. Stress decay, pulse duration, release structure and wave dispersion are very well defined by these measurements. Free surface velocity measurements at the rod end basically provide the strength of the transmitted compressive wave and the pull back signal due to bar spalling. In making dynamic yield strength estimates, the average level of the free surface particle velocity which follows the arrival of the second compressive wave should be used. The lower velocity level that follows corresponds to the pulse strength trap at the bar end which is a function of the pulse tail strength. A more damage sensitive free surface velocity measurement is the radial velocity. When such measurements are performed within two bar diameters from the impact plane, the rate of damage and its distribution can be recorded. The duration of these records is expected to be limited due to severe surface degradation after approximately 10 μs, especially at points very close to the impact surface.

High speed photography is instrumental in the understanding of failure modes. It is shown that unconfined alumina bars fail by stress induced microcracking. The overall agreement between the numerical simulations and the experimental records clearly indicates that the microcracking multiple-plane model has the potential to capture the main physics of the dynamic failure process. Quantitative characterizations of microcrack densities, initial size distribution, and nucleation rates are not available. However, it should be emphasized that while the quantitative predictions would depend on these parameters, the main qualitative features are not expected to.

We have confined attention to a multiple-plane microcracking model in which a plastic-like behavior of the material due to second phases is not directly included. The model could in principle be extended to account for this effect (Curran *et al.*, 1992; Espinosa, 1992), although there is not enough information on the mechanical behavior of these grain boundary phases. The presence of glass at the interfaces determines the early stages of inelasticity and acts as a precursor for the development of microcracks. By contrast, high purity ceramics possess tougher interfaces, and cracks are nucleated due to plastic deformation within the grains (slip, twining). It is clear that a detailed and complete description of the failure of brittle materials under multiaxial loading requires coupling between plasticity, densification (in the case of ceramics containing a glassy phase), and microcracking. This and other key issues like microcrack densities and nucleation rates need to be addressed in order to develop general models of brittle failure.

ACKNOWLEDGEMENTS

This research was supported by the National Science Foundation through Grant No. MSS-9309006, and by the Purdue Research Foundation through Grant No. 690-1282-2001. The experimental work was sponsored by the U.S. Army Research Office under contract DAAL03-

88-K-0203. Stephan Bless of The Institute for Advanced Technology of The University of Texas at Austin is sincerely thanked for sharing the data for shots 7-1748 and 7-1750.

REFERENCES

Bazant, Z. P. and Gambarova, P. G. (1984) Crack shear in concrete: crack band microplane model. *J. Struct. Engng, ASCE* **110**(9), 2015–2035.

Brar, N. S. and Bless, S. J. (1992) Dynamic fracture and failure mechanisms of ceramic bars. *Shock-Wave and High-Strain-Rate Phenomena in Materials* (ed. M. Meyer *et al.*). Marcel Dekker, NY.

Curran, D. R., Seaman, L., Cooper, T. and Shockey, D. A. (1993) Micromechanical model for comminution and granular flow of brittle material under high strain rate. Application to penetration of ceramic targets. *Int. J. Impact Engng* **13**(1), 53–83.

Espinosa, H. D. (1989) Finite element analysis of stress induced damage in ceramics. MSc. Thesis, Brown University, Providence, RI.

Espinosa, H. D. (1992) Micromechanics of the dynamic response of ceramics and ceramic composites. PhD. Thesis, Brown University, Providence, RI.

Espinosa, H. D. (1994) On the dynamic shear resistance of ceramic composites and its dependence on multiaxial deformation. To appear in *Int. J. Solids Struct.*

Espinosa, H. D. and Clifton, R. J. (1991) Plate impact experiments for investigating inelastic deformation and damage of advanced materials. *Symp. Experiments in Micromechanics of Fracture-Resistant Materials* (ed. Kim K. S.), pp. 37–56. ASME Winter Annual Meeting.

Espinosa, H. D., Raiser, G., Clifton, R. J. and Ortiz, M. (1992) Experimental observations and numerical modeling of inelasticity in dynamically loaded ceramics. *J. Hard Mater.* **3**(3–4), 285–313.

Freund, L. B. (1990) *Dynamic Fracture Mechanics*. Cambridge University Press, Cambridge.

Grady, D. and Wise, J. L. (1993) Dynamic properties of ceramic materials. *Sandia Report*, SAND93-0610.

Ju, J. W. and Lee, X. (1991a) On three dimensional self-consistent micromechanical damage models for brittle solids. Part I: tensile loadings. *J. Engng Mech. ASCE* **117**(7), 1495–1514.

Ju, J. W. and Lee, X. (1991b) On three dimensional self-consistent micromechanical damage models for brittle solids. Part II: compressive loadings. *J. Engng Mech., ASCE* **117**(7), 1515–1536.

Kachanov, M. (1980) Continuum model of medium with cracks. *J. Engng Mech. Div., ASCE* **106**(EM5), 1039–1051.

Kipp, M. and Grady, D. (1989) Shock compression and release in high-strength ceramics. Sandia Report, SAND89-1461.

Longy, F. and Cagnoux, J. (1989) Plasticity and microcracking in shock-loaded alumina. *J. Am. Ceram. Soc.* **72**(6), 971.

Needleman, A. (1988) Material rate dependence and mesh sensitivity in localization problems. *Comput. Meth. Engng* **67**, 69.

Rajendran, A. M. (1992) High strain rate behavior of metals, ceramics, and concrete. *Air Force Report WL-TR*-92-4006, Wright-Patterson Air Force Base, OH.

Rosenberg, Z. and Partom, Y. (1985) Longitudinal dynamic stress measurements with in-material piezoresistive gauges. *J. Appl. Phys.* **58**(5), 1814–1818.

Rosenberg, Z., Brar, N. S. and Bless, S. J. (1988) Elastic precursor decay in ceramics as determined with manganin stress gauges. *J. Physique* **C3**, 707.

Sandler, I. S. and Wright, J. P. (1984) Strain-softening. *Theoretical Foundations for Large Scale Computations of Nonlinear Materials Behavior* (ed. Nemat Nasser *et al.*), pp. 285. Martinus Nijhoff.

Seaman, L. and Dein, J. L. (1983) Representing shear band damage at high strain rates. *Proceeding of the IUTAM Symposium on Nonlinear Deformation Waves*, Tallin, Estonia. Springer-Verlag, Berlin.

Seaman, L., Curran, D. R. and Crewdson, R. C. (1978) Transformation of observed crack traces on a section to true crack density for fracture calculations. *J. Appl. Phys.* **49**(10), 5221.

Willis, I. R. (1968) The stress field around an elliptical crack. *Int. J. Engng Sci.* **6**(5), 253–263.

Winkler, W. D. and Stilp, A. J. (1992) Pressure induced macro- and micromechanical phenomena in planar impacted TiB_2. *Shock Compression of Condensed Matter*-1991 (ed. S. C. Schmidt, R. D. Dick, J. C. Forbes and D. G. Tasker), pp. 555. Elsevier Science Publishers, Amsterdam.

Yeshurun, Y., Brandon, D. G. and Rosenberg, Z. (1987) Impact damage mechanisms in debased alumina. *Proc. of the IMPACT* 87 *Conference*, Bremen, FRG.

Zienkiewicz, O. C. and Taylor, R. L. (1989) *The Finite Element Method.* McGraw-Hill, London.